

Unveiling the role of RhoA and ferroptosis in vascular permeability: Implications for osteoarthritis

XIAOXIN HE^{1*}, KUANMIN TIAN^{1*}, XUE LIN², XIAOLEI CHEN¹, YAJING SU², ZHIDONG LU³,
ZHIRONG CHEN³, LIANG ZHANG³, PENG LI³, LONG MA³, GANGNING FENG⁴,
XIN ZHAO³, ZHIBIN LAN¹, CHEN ZHANG⁵, DI XUE^{2,6} and QUNHUA JIN^{2,3}

¹First Clinical Medical College, Ningxia Medical University, Yinchuan, Ningxia Hui 750004, P.R. China;

²Institute of Medical Sciences, General Hospital of Ningxia Medical University, Yinchuan, Ningxia Hui 750004, P.R. China;

³Orthopedics Ward 3, The General Hospital of Ningxia Medical University, Yinchuan, Ningxia Hui 750004, P.R. China;

⁴Ningxia Institute of Osteoarthropathy, General Hospital of Ningxia Medical University, Yinchuan, Ningxia Hui 750004, P.R. China;

⁵School of Education, Ningxia University, Yinchuan, Ningxia Hui 750004, P.R. China; ⁶Ningxia Key Laboratory of Clinical and Pathogenic Microbiology, General Hospital of Ningxia Medical University, Yinchuan, Ningxia Hui 750004, P.R. China

Received January 25, 2024; Accepted May 8, 2024

DOI: 10.3892/ijmm.2024.5410

Abstract. Abnormal angiogenesis and increased vascular permeability of subchondral bone are key mechanisms related to osteoarthritis (OA). However, the precise mechanisms responsible for heightened vascular permeability in OA remain unclear. The present study used proteomics to identify protein expression in damaged subchondral bone compared with normal subchondral bone. The results suggest that Ras homolog family member A (RhoA) may be associated with the vascular permeability of subchondral bone and ferroptosis in OA. The results of analysis of clinical samples indicated a significant increase in expression of RhoA in the subchondral bone of OA. This was consistent with the proteomics findings. We found through western blotting, RT-PCR, and immunofluorescence that RhoA significantly increased the permeability of endothelial cells (ECs) by inhibiting inter-EC adhesion proteins (zona occludens-1, connexin 43 and Vascular endothelial-Cadherin) and actin filaments. Furthermore, RhoA induced ferroptosis core proteins (glutathione peroxidase 4, solute carrier family 7 member 11 and acyl-CoA synthase long-chain family member 4, ACSL4) by influencing lipid peroxidation and mitochondrial function, leading to ferroptosis of ECs. This suggested an association between RhoA,

ferroptosis and vascular permeability. Ferroptosis significantly increased permeability of ECs by inhibiting inter-EC adhesion proteins. RhoA increased vascular permeability by inducing ferroptosis of ECs. *In vivo*, inhibition of RhoA and ferroptosis significantly mitigated progression of OA by alleviating cartilage degeneration and subchondral bone remodeling in mice with destabilization of the medial meniscus. In conclusion, the present findings indicated that RhoA enhanced vascular permeability in OA by inducing ferroptosis. This may serve as a novel strategy for the early prevention and treatment of OA.

Introduction

Osteoarthritis (OA) is the most prevalent degenerative joint disease globally and the primary cause of joint pain, discomfort and limited activity among middle-aged and elderly individuals. As of 2019, ~250 million people worldwide were affected (1,2). During OA progression, new blood vessels form in the subchondral bone, extend to the tidemark and infiltrate the avascular cartilage. Notably, an increase in the permeability of these new blood vessels promotes infiltration of various inflammatory factors into the cartilage, which exacerbates cartilage degeneration and OA severity (3,4). Additionally, studies have indicated that inhibiting formation of new blood vessels and reducing permeability in subchondral bone can mitigate progression of OA (5,6). However, the specific mechanism underlying increased vascular permeability in the subchondral bone during OA remains elusive.

Vascular permeability primarily depends on adhesive connections and tight junctions between endothelial cells (ECs) (7,8). RhoA is a member of the Rho GTP family and plays a key role in governing the rearrangement of the cytoskeleton and intercellular junctions of ECs (9,10). RhoA enhances retinal vascular permeability by inhibiting the junctions between ECs (11). Additionally, RhoA induces EC apoptosis and amplifies EC permeability in rats with chronic renal failure (12). However, it remains uncertain whether

Correspondence to: Professor Qunhua Jin or Dr Di Xue, Institute of Medical Sciences, General Hospital of Ningxia Medical University, 878 Shengli Road, Yinchuan, Ningxia Hui 750004, P.R. China

E-mail: jinqunhua20202020@163.com

E-mail: xue_di@yeah.net

*Contributed equally

Key words: osteoarthritis, RhoA, ferroptosis, vascular permeability

RhoA influences the vascular permeability of the subchondral bone in OA. Comprehensive understanding of the mechanism of RhoA in the pathogenesis of OA may facilitate the development of prevention and treatment strategies.

Ferroptosis is a form of cell death. During ferroptosis, the antioxidant axis of solute carrier family 7 member 11/glutathione peroxidase 4 (SLC7A11/GPX4) is deactivated, resulting in intracellular oxidative stress. An increase in oxidative stress upregulates lipid peroxidation and induces programmed cell death, with acyl-CoA synthase long-chain family member 4 (ACSL4) serving a key role (13–15). Ferroptosis influences vascular permeability (16). For example, inhibiting ferroptosis in ECs preserves the integrity of the blood-spinal cord barrier and enhances spinal cord injury recovery (17). Additionally, upregulation of lipid peroxidation and inflammatory responses in retinal vascular ECs prompt EC dysfunction and increase permeability (18). However, the role and molecular mechanisms of RhoA in OA are yet to be elucidated. Therefore, the present study aimed to investigate the role and molecular mechanisms of RhoA in OA, EC ferroptosis and vascular permeability.

Materials and methods

Patients and specimens. The present study was approved by the Ethics Committee of General Hospital of Ningxia Medical University (Yinchuan, China; approval no. KYLL-2021-269) and all experimental procedures adhered to the Declaration of Helsinki. Human subchondral bone samples were obtained from individuals undergoing total knee arthroplasty. Written informed consent was provided by the patients.

Tibial plateau samples were collected from 60 patients (male:female ratio, 1:3; age range, 58–82) diagnosed with knee OA and undergoing total knee arthroplasty at the General Hospital of Ningxia Medical University, China, between February 2022 and February 2023. The subchondral bone was categorized into damaged area (OA sample) and corresponding undamaged area (control sample). OA diagnosis was based on diagnostic criteria of the American Rheumatology Association (19). Patients with secondary OA, such as those with trauma or connective tissue disease, were excluded.

Animal model. In total, 60 healthy adult female C57BL/6 mice (age: 6 weeks; weight: 16g) were acquired from the Experimental Animal Center of Ningxia Medical University, China. Mice were maintained in a specific pathogen-free environment under standard conditions (22±1°C, 55% humidity and 12/12-h light/dark cycle) with free access to food and water. Destabilization of the medial meniscus (DMM) was induced in the right knee joint to establish the OA model. All mice were randomly divided into four groups (n=15 mice/group): Control (sham-operated), OA (DMM), ferrostatin-1 (DMM + ferrostatin-1) and rhosin (DMM + rhosin). After anesthetizing mice with an intraperitoneal injection of pentobarbital (40 mg/kg), incisions were made in the skin and joint cavity. The meniscus ligament of the right knee joint was transversely cut to release the meniscus anterior segment. In the control group, the meniscus ligament was left intact (20). Mice in the DMM + ferrostatin-1 and DMM + rhosin groups received intraperitoneal ferrostatin-1 (15 mg/kg) and rhosin (40 mg/kg), respectively, twice/week (21,22), while mice

in the control and DMM groups were administered an equivalent volume of normal saline on the same schedule. At 4 and 8 weeks after surgery, mice were anesthetized via intraperitoneal injection of pentobarbital (40 mg/kg) and blood samples (volume, 0.4 ml) were collected using the cardiac puncture method for biochemical analysis. Subsequently, mice were sacrificed via cervical dislocation. The knee joint, liver, kidney and spleen tissues were harvested for further experiments at 8 weeks after surgery. The animal experimental procedure is illustrated in Fig. 1.

Isolation and culturing of ECs from bone. Briefly, six healthy adult female C57BL/6 mice (age, 6 weeks; weight, 16 g) were acquired from the Experimental Animal Center of Ningxia Medical University, China. Mice were maintained in a specific pathogen-free environment under standard conditions (22±1°C, 55% humidity and 12/12-h light/dark cycle) with free access to water and food. Mice were anesthetized via intraperitoneal injection of pentobarbital (40 mg/kg), followed by sacrifice via cervical dislocation. Femur and tibia bones were collected from mice and preserved in sterile PBS devoid of Ca²⁺ and Mg²⁺. The bones were ground using a mortar and pestle and digested with collagenase (Sigma-Aldrich; Merck KGaA) to achieve a single-cell suspension. ECs were isolated from the cell suspension using Magnetic-Activated Cell Sorting (MACS) with CD31 antibody (50 µg/5x10⁷ cells; cat. no. ab7388; Abcam) for 15 min at 4°C. The sorted ECs were seeded (1x10⁶) in a culture dish pre-coated with fibronectin (cat. no. 354403; Corning, Inc.), followed by the addition of endothelial cell growth medium (EBM-2) supplemented with EGM-2 SingleQuots (CC-4176; both Clonetics; Lonza), cells were maintained in a humidified environment at 37°C under a 5% CO₂ atmosphere for 48 h. During the first passage, the cells were sorted with CD31 antibody using MACS sorting kit (cat. no. 11061D; Thermo Fisher Scientific, Inc.) according to the manufacturer's instructions. Cells were maintained in a humidified environment at 37°C under a 5% CO₂ atmosphere for 48 h. ECs between the second and fifth passages were used for subsequent experiments. ECs were stimulated with interleukin-1β (100 ng/ml) for 24 h with or without 50 µM ferroptosis inhibitor ferrostatin-1 or 10 µM ferroptosis activator erastin at 37°C (all MedChemExpress).

Transfection. Lentiviral vectors (psi-LVRU6P) were purchased from GeneCopoeia to stably knock down RhoA in ECs. The lentiviral vectors include RhoA (MSH031463-LVRU6P) and scrambled short hairpin (sh)RNA as the negative control (CSHCTR001-LVRU6P). Briefly, 293T cells (cat. no. CL-0005; Pricella) were transfected with 10 µg lentivirus vector using calcium phosphate method (23). The concentration of the plasmid is 166 ng/µl. We used a transfection reagent (Lipofectamine 3000; cat. no. L3000001; Thermo Fisher Scientific Inc.). Following 48 h incubation at 37°C, the viral supernatant was collected and filtered. ECs were incubated overnight with the supernatant at 37°C, followed by the addition of 10 µg/ml polybrene. RhoA knockdown cells were selected using 2 µg/ml puromycin. Subsequently, cells were continuously screened with medium containing 2 µg/ml puromycin and passaged for three generations to maintain stable expression, which were then preserved. Subsequent

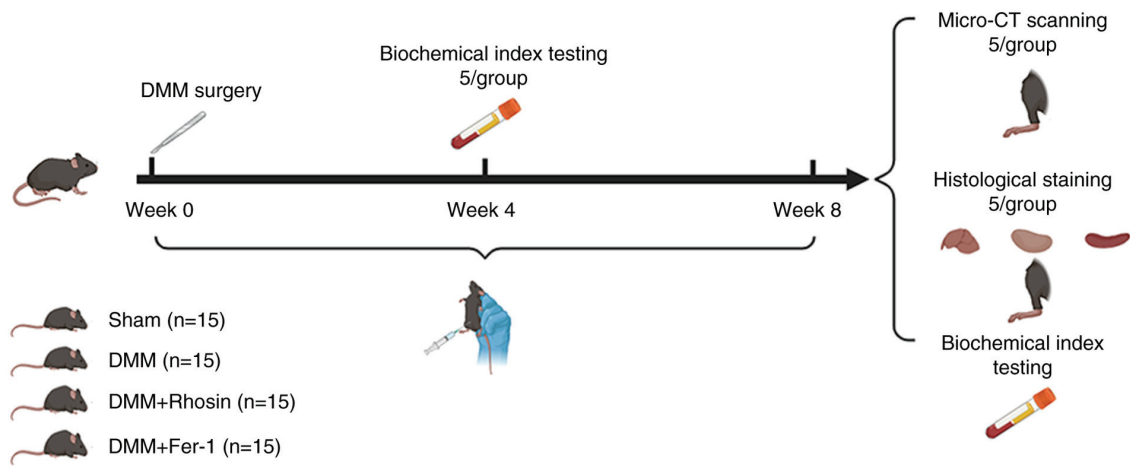


Figure 1. Animal experiment workflow. Mice were randomly divided into four groups (n=15/group) and sampled at 4 and 8 weeks for serum and histological examination. DMM, destabilization of the medial meniscus; CT, micro-computed tomography; Fer, Ferrostatin-1.

experiments will be conducted after 1 week. shRNA and the negative control sequence are listed in Table SI.

Reverse transcription-quantitative (RT-q) PCR. Total RNA was extracted from ECs using TRIzol (Thermo Fisher Scientific, Inc.) according to the manufacturer's instructions. RNA (1 μ g) was reverse-transcribed to cDNA using a PrimeScript RT reagent kit (cat. no. RR037A; Takara Bio, Inc.) according to the manufacturer's instructions. qPCR was performed on a MiniOpticon real-time PCR system (Bio-Rad Laboratories, Inc.) using the TB Green Detection kit (Takara Bio, Inc.) and specific primers (Table SII) with β -actin as the internal control. Thermocycling conditions include a Holding Stage (reps: 1; 95°C; 30 sec) and a Cycling Stage (Number of Cycles: 40; 95°C 3 sec; 60°C 12 sec to 15 sec * 2). The relative expression of the target genes was calculated using the $2^{-\Delta\Delta C_q}$ method and normalized to that of β -actin (24). All reactions were performed in quintuplicate.

Western blotting. Briefly, ECs were seeded in 6-well plates at a density of 5×10^5 /well and incubated with IL-1 β (100 ng/ml) for 24 h in the presence or absence of 50 μ M ferroptosis inhibitor ferrostatin-1 or 10 μ M ferroptosis activator erastin at 37°C. Following three washes with PBS, protein was extracted from the cells on ice using 80 μ l Mammalian Protein Extraction Reagent (Thermo Fisher Scientific, Inc.). The protein concentration was determined using the BCA method. Thereafter, proteins (30 μ g/lane) from each sample were separated using 10/15% SDS-PAGE and transferred to PVDF membranes. After blocking with 5% skimmed milk for 1 h at room temperature, membranes were incubated with specific primary antibodies overnight at 4°C. After five washes with TBST (0.05% Tween), the membranes were incubated with the secondary antibody for 1 h at room temperature. Protein bands were visualized using an enhanced chemiluminescent (ECL) kit (cat. no. RM0021; ABclonal) and images were captured using ChemiDoc™ Imaging Systems (Bio-Rad Laboratories, Inc.). The expression levels of the proteins were quantified using ImageJ v1.8.0 software (National Institutes of Health). The following primary

antibodies were used: Ras homolog family member A (RhoA; 1:2,000; cat. no. ab187027; Abcam), zona occludens-1 (ZO-1; 1:1,000; cat. no. ab96587; Abcam), connexin 43 (1:1,000; cat. no. ab235282; Abcam), intercellular adhesion Molecule-1(ICAM-1; 1:500; cat. no. ab171123; Abcam), glutathione peroxidase 4 (GPX4; 1:1,000; cat. no. ab125066; Abcam), solute carrier family 7 member 11 (SLC7A11; 1:1,000; cat. no. ab307601; Cell Signaling Technology, Inc.), acyl-CoA synthase long-chain family member 4 (ACSL4; cat. no. 22401-1-AP; Proteintech Group, Inc.), tumor necrosis factor- α (TNF- α ; cat. no. 11948; Cell Signaling Technology, Inc.) and β -actin (1:1,000; cat. no. 66009-1-Ig; Proteintech Group, Inc.). The following secondary antibodies were used: Horseradish peroxidase-conjugated goat anti-rabbit (1:10,000; cat. no. ab205718; Abcam) and anti-mouse IgG (1:10,000; cat. no. ab205719; Abcam).

Cell viability assay. Briefly, the viability of ECs was assessed using a Cell Counting Kit-8 (CCK-8) assay (Dojindo Laboratories, Inc.). ECs were seeded in 96-well plates at a density of 3,000 cells/well (six replicate wells for each condition), followed by treatment with IL-1 β (0, 1, 10, 100, 200, 500 and 1,000 ng/ml), ferrostatin-1 (0, 1, 10, 50, 100 and 200 μ M) or erastin (0, 1, 5, 10, 50, 100 μ M) alone for 24, 48, 72 h at 37°C. After discarding the medium, 100 μ l 10% CCK-8 solution was added to each well, followed by incubation at 37°C for 1 h. The absorbance was measured at 460 nm using an enzyme-linked instrument (Infinite® 200 PRO; Tecan Group, Ltd.).

Wound healing assay. ECs were evenly seeded (5×10^5 /well) into 6-well plates and incubated for 12 h at 37°C. Thereafter, scratches were formed on the EC monolayer and cultured using serum-free medium, followed by treatment with interleukin-1 β (100 ng/ml) with or without 50 μ M ferroptosis inhibitor ferrostatin-1 or 10 μ M ferroptosis activator erastin for 24 h at 37°C in 5% CO₂. The confluence on either side of the wound is 1×10^6 /well. Images were captured using a fluorescence microscope (cat. no. BX53; Olympus Corporation) at 0 and 24 h. The extent of cell migration was quantified by comparing the remaining wound area with the area at 0 h post-scratch.

Fluorescence analysis. ECs were treated with IL-1 β (100 ng/ml) for 24 h with or without 50 μ M ferroptosis inhibitor ferrostatin-1 or 10 μ M ferroptosis activator erastin at 37°C, rinsed with PBS, fixed with 4% paraformaldehyde for 10 min and permeabilized with 0.1% Triton X-100 (Beyotime Institute of Biotechnology) for 5 min at 25°C. After three washes with PBS, the cells were blocked with 1% BSA (Beijing Solarbio Science & Technology Co., Ltd.) for 30 min at 25°C. For immunofluorescence assay, ECs were incubated with primary antibodies overnight at 4°C, followed by incubation with secondary antibodies in the dark at room temperature for 2 h. For phalloidin staining, ECs were incubated with 200 μ l Tetramethylrhodamine Isothiocyanate Phalloidin working solution (100 nM; Beijing Solarbio Science & Technology Co., Ltd.) in the dark for 30 min at 25°C. To assess lipid peroxidation and mitochondrial membrane potential, cells were incubated in the dark with 200 μ l Liperfluo working solution (1 μ M; Invitrogen; Thermo Fisher Scientific, Inc.) for 30 min at 37°C, followed by incubation in the dark with Rhodamine 123 working solution (2 μ M; Beyotime Institute of Biotechnology) for 15 min at 37°C. Following thorough washing with PBS, nuclei were stained with DAPI (5 μ M; Invitrogen; Thermo Fisher Scientific, Inc.) for 30 min at 25°C and sealed. The primary antibodies were as follows: RhoA (1:200; cat. no. ab187027; Abcam), ZO-1 (1:500; cat. no. ab96587; Abcam), connexin 43 (1:200; cat. no. ab235282; Abcam), GPX4 (1:200; cat. no. ab125066; Abcam), ACSL4 (1:300; cat. no. 22401-1-AP; Proteintech) and VE-cadherin (1:400; cat. no. 2500T; Cell Signaling Technology, Inc.). Fluorescence signals were visualized using a fluorescence microscope (cat. no. BX53; Olympus Corporation) and analyzed using ImageJ v1.8.0 software (National Institutes of Health). Brightness and contrast adjustments were performed during image processing. For consistent comparison, all images were captured using identical collection settings.

Histology and immunohistochemical (IHC) staining. The knee joint, liver, kidney and spleen tissue was fixed in 4% paraformaldehyde buffer for 24 h at 4°C and decalcified in 10% EDTA for 4 weeks at 25°C. After dehydration with graded ethanol, tissues were embedded in paraffin, sectioned (thickness, 4 μ m) and subjected to hematoxylin and eosin (H&E), safranin-O-fast green and Masson staining. According to the instructions of the H&E staining kit (cat. no. G1076; Servicebio Technology), the sections were dewaxed and dehydrated, then stained with hematoxylin followed by eosin staining (both 5 min at 20°C). For safranin O-fast green staining (cat. no. G1053; Servicebio Technology), the deparaffinization of slides was consistent with the description above. Subsequently, they were stained with Fast Green for 6 min, washed at 20°C, dehydrated, and then stained with Safranin O at 20°C for 3 min. The Osteoarthritis Research Society International (OARSI) scoring system was used to evaluate the degeneration of articular cartilage (25). The distance from the tidemark to the surface of the articular cartilage was measured and recorded as the thickness of the hyaline cartilage (HC), while the distance from the tidemark to the subchondral bone plate was recorded as the thickness of the calcified cartilage (CC). For Masson staining (cat. no. G1006; Servicebio Technology), sections were soaked in 2.5% potassium dichromate staining solution overnight at 25°C and incubated for 30 min at 65°C. Next, the sections were

immersed in Weigert's iron hematoxylin staining solution for 1 min, followed by staining in Van Gieson's acid fuchsin for 6 min at 25°C. Subsequently, the sections were immersed in 1% phosphomolybdic acid solution for 1 min, and then stained in 2.5% aniline blue solution for 30 sec at 25°C. For IHC, tibial plateau samples were prepared as aforementioned. Following dewaxing and rehydration, 0.1% trypsin was used for antigen retrieval at 37°C for 30 min. Subsequently, endogenous peroxidase activity was quenched with 3% hydrogen peroxide for 10 min at 25°C. After blocking with 5% normal goat serum (cat. no. G1208; Servicebio Technology) at 37°C for 30 min, the sections were incubated overnight at 4°C with the following primary antibodies: RhoA (1:300; cat. no. ab54835; Abcam), ZO-1 (1:500; cat. no. ab221547; Abcam), GPX4 (1:250; cat. no. ab125066; Abcam) and ACSL4 (1:500; cat. no. 22401-1-AP; Proteintech Group, Inc.). The secondary antibodies were used: Horseradish peroxidase-conjugated goat anti-rabbit (1:10,000; cat. no. ab205718; Abcam) and anti-mouse IgG (1:10,000; cat. no. ab205719; Abcam) for 30 min at 25°C. The sections were stained using DAB (cat. no. G1212; Servicebio Technology) and counterstained with hematoxylin for 5 min at 25°C. Images were captured using an optical microscope (cat. no. CX43; Olympus Corporation) and analyzed using ImageJ v1.8.0 software (National Institutes of Health).

Micro-computed tomography (Micro-CT) analysis. After removing the surrounding skin and muscles, the right knee joint of the mice was fixed with 4% paraformaldehyde at room temperature for 48 h. Scans were performed using a micro-CT (SkyScan 1176; Bruker Belgium S.A./N.V.) with a resolution of 9 μ m/pixel. Analyzed indices included bone volume fraction (BV/TV), trabecular separation (Tb.Sp), trabecular thickness (Tb.Th) and tissue mineral density (TMD).

Determination of serum biochemical indexes. The acquired mouse whole blood sample was centrifuged at 3,000 rpm for 15 min, and the supernatant was collected as the serum sample. This was stored at -80°C for subsequent use. Working solutions were prepared according to the guidelines of the reagent manufacturer (cat. no. BC2, BC4, BC5, BC7; LWPOCT). Biochemical indices, including Albumin (ALB), Direct bilirubin (DBIL), Total bile acids (TBA), Triglycerides (TG), Total cholesterol (TC), High-density lipoprotein cholesterol (HDL-C), Low-density lipoprotein cholesterol (LDL-C), Glucose (GLU), Glycated serum protein (GSP), Creatine kinase (CK), Creatine kinase-MB (CK-MB), Lactate dehydrogenase (LDH), Hydroxybutyrate dehydrogenase (HBDH), Superoxide dismutase (SOD), UREA, Creatinine (CRE), and Uric acid (UA) were assessed using an automatic biochemical analyzer, and the results were documented. Serum indices for Malondialdehyde (MDA), glutathione (GSH), and Total antioxidant capacity (T-AOC) in mice were determined based on the kit's instructions (cat. no. A003-1, A006-2-1, A015-2-1; Jiancheng), with the final data obtained using the microplate reader (cat. no. Epoch; Bio TEK).

Liquid chromatography-tandem mass spectrometry (LC-MS/MS) and label-free quantification of tissue proteomes. Paired OA and control tissue samples from 30 patients were

combined at a ratio of 10:1, after which the tissue proteins were subjected to LC-MS/MS for label-free quantification. LC-MS/MS analysis was performed on a Q Exactive mass spectrometer coupled to Easy nLC (Thermo Fisher Scientific, Inc.). The mass spectrometer was operated in positive ion mode. The nitrogen gas temperature is 180°C with a flow rate of 3 l/min. Parallel reaction monitoring (PRM) transitions assessed are within the 300-1,800 scan range. LC-MS/MS was used for data collection, followed by a database search (uniprot.org) to identify proteins. Adjusted $P < 0.05$ and Log (Fold Change) > 1 or Log (Fold Change) < -1 were defined as the threshold for the differential expression of protein. Gene Ontology (GO; <https://www.geneontology.org>) functional annotation and Kyoto Encyclopedia of Genes and Genomes (KEGG; <http://geneontology.org/>) pathway enrichment analysis were performed on the DEPs. The results were plotted by R (version: 4.3.3) software (<https://www.r-project.org>).

Statistical analysis. All data are presented as the means \pm SD. All independent experiments were repeated at least three times. All statistical analyses were performed using GraphPad Prism 9.0 (GraphPad Software, Inc.; Dotmatics). Statistical comparisons between two groups were performed using unpaired Student's *t* test. For ≥ 3 groups, a variance homogeneity test was first conducted, followed by one-way ANOVA and Tukey's multiple comparison post hoc test. $P < 0.05$ was considered to indicate a statistically significant difference.

Results

RhoA is highly expressed in the OA clinical samples. The present study analyzed age, BMI, Visual Analog Scale (VAS) score, Lysholm score, WOMAC (Western Ontario and McMaster Universities Osteoarthritis Index) score and Kellgren-Lawrence (K-L) grades of the 60 clinical samples (Fig. S1A-F) from 30 patients with OA who had not received any drugs. Pre- and postoperative anteroposterior and lateral radiographs and preoperative MRI scans were performed (Fig. S1G). Overall, the average age was 68.72 ± 7.941 years. The BMI was 27.22 ± 1.480 . The VAS score was 7.15 ± 1.424 , the Lysholm score was 76.43 ± 8.001 , and the WOMAC score was 46 ± 7.105 . All patients had a K-L grade of 3-4, consistent with characteristics of OA.

Bioinformatics analysis of the proteome data showed 292 DEPs in the OA vs. control group, among which RhoA was significantly upregulated (Fig. 2A and B). KEGG analysis indicated that most DEPs were enriched in processes such as 'cell migration' (Fig. S2B). GO analysis showed that the DEPs were primarily enriched in biological processes associated with 'PPAR signaling pathway', 'ferroptosis' and 'pentose phosphate pathway' (Fig. S2A). Overall, these results suggested that RhoA may be associated with these biological processes.

Furthermore, H&E and safranin-O-fast green staining indicated noticeable subchondral bone remodeling and sclerosis in clinical samples of OA (Fig. 2C-F). IHC showed a significantly higher expression of RhoA in OA than in undamaged subchondral bone (Fig. 2G and K). Collectively, these results indicated that RhoA was upregulated in the subchondral bone remodeling phase of OA.

GPX4 and vascular adhesion are significantly downregulated in OA samples, while ACSL4 significantly upregulated. To investigate ferroptosis in OA, expression of GPX4 and ACSL4, key regulators of ferroptosis (26), was assessed in OA and undamaged tissue. There was a significant decrease in GPX4 expression and an increase in ACSL4 expression in OA-damaged tissue (Fig. 2H, I, L and M). To determine whether there was an alteration in vascular permeability during OA development, expression of the cell adhesion molecule ZO-1 was assessed (27,28). ZO-1 expression was significantly downregulated in OA compared with controls (Fig. 2J and N). Overall, these results indicated GPX4 and vascular adhesion are significantly downregulated during OA progression, while ferroptosis core factor-ACSL4 significantly upregulated.

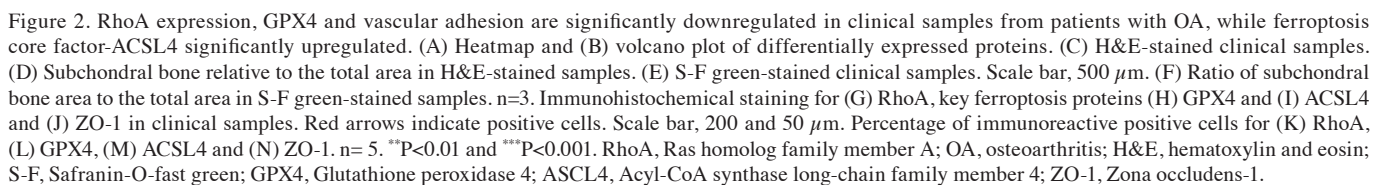
RhoA enhanced the permeability of ECs. Ferrostatin-1 and erastin are inhibitors and activators of ferroptosis, respectively (29). Cell viability assay was performed to examine cytotoxic effects of IL-1 β , ferrostatin-1 and erastin on ECs. IL-1 β , ferrostatin-1 and erastin were not cytotoxic to ECs at concentrations < 100 ng/ml and 50 and 10 μ M, respectively. Notably, there was no significant difference in cell viability at 24, 48 and 72 h of treatment (Fig. S3A-I).

To investigate changes in RhoA expression in IL-1 β -treated ECs, EC lentiviral transduction was performed. Successful lentiviral transduction of ECs inhibited expression of RhoA at the protein and mRNA levels (Fig. S4A-C). RhoA knockdown significantly inhibited IL-1 β -induced increase in RhoA expression in ECs, evidenced by a decrease in the fluorescence intensity of RhoA following RhoA knockdown (Fig. S4D and E). Additionally, western blotting indicated that RhoA knockdown significantly reversed IL-1 β -induced increase in RhoA protein expression in ECs (Fig. S4F and G), which was confirmed by RT-qPCR (Fig. S4H). Collectively, these results suggested that IL-1 β increased RhoA expression in ECs but this effect was reversed by RhoA knockdown.

To elucidate the effect of RhoA on inflammatory responses in ECs, mRNA expression of inflammatory genes in ECs was assessed. RhoA knockdown significantly attenuated IL-1 β (100 ng/ml)-induced increase in mRNA expression of ICAM1, VCAM1, MCP-1, TNF- α , IL-6 and IFN- γ (Fig. S5A-F). Additionally, RhoA knockdown suppressed IL-1 β -induced increase in protein expression of TNF- α and ICAM1 in ECs (Fig. S5G-I). Overall, these results suggested that RhoA knockdown ameliorated inflammatory response in ECs.

The role of RhoA in the expression of vascular permeability-related markers was assessed. ZO-1 and connexin 43, which are key factors for adhesion and connection between ECs, inhibit vascular permeability (30,31). Immunofluorescence staining revealed RhoA knockdown significantly reversed IL-1 β -induced decrease in the mean fluorescence intensity of ZO-1 and connexin 43 (Fig. 3A-D). RT-qPCR showed that RhoA knockdown enhanced IL-1 β -induced decrease of ZO-1 and connexin 43 mRNA levels in ECs (Fig. 3E and F), which was confirmed by western blot analysis (Fig. 3G-I).

To elucidate the influence of RhoA on vascular permeability, actin cytoskeleton and VE-cadherin staining was performed. The actin cytoskeleton interacts with VE-cadherin to regulate integrity of intercellular connections (32). IL-1 β treatment significantly decreased stress fibers within ECs but increased



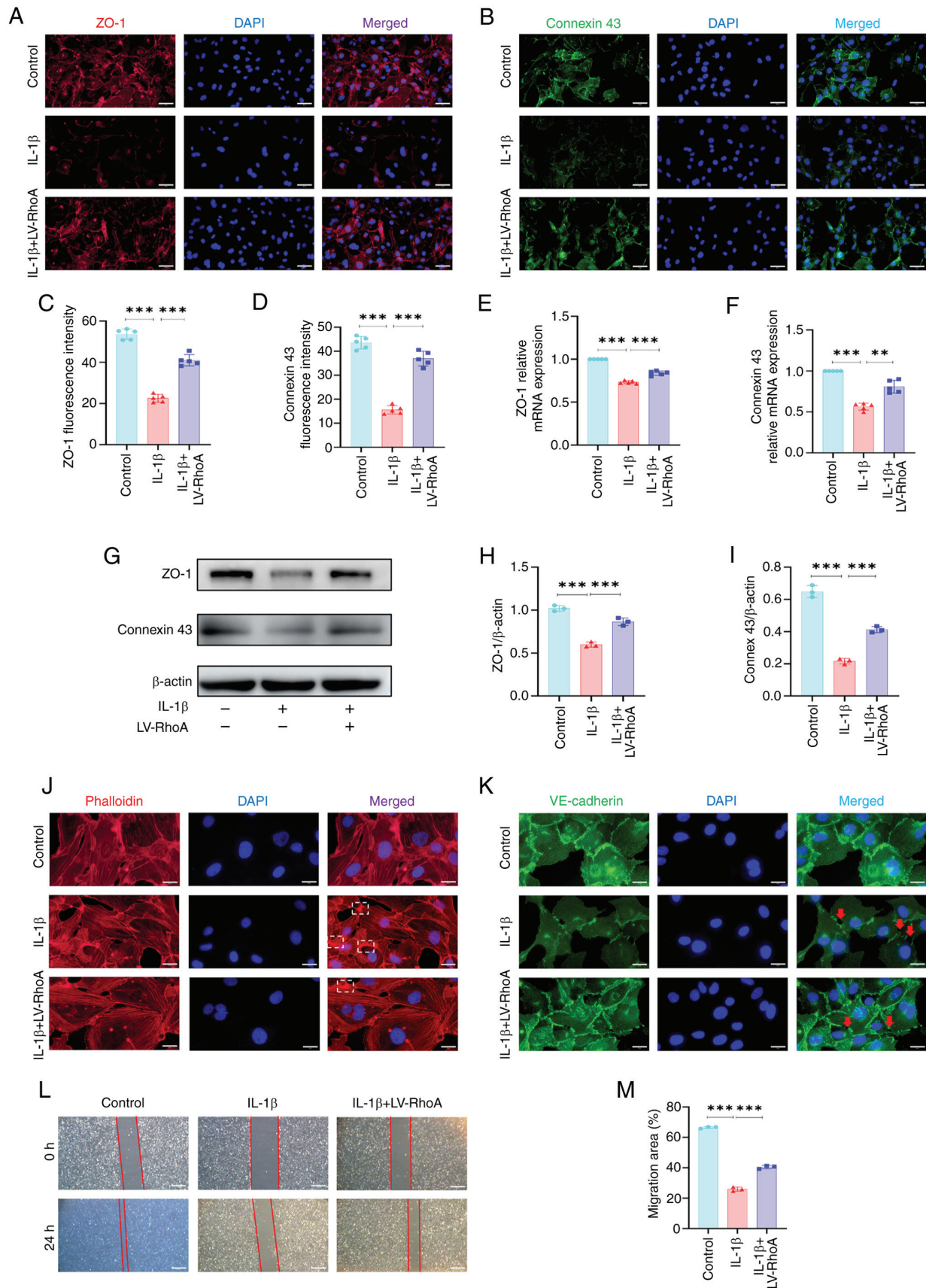


Figure 3. RhoA inhibition reverses IL-1 β -induced increase in EC permeability. ECs were transfected with LV-RhoA and treated with or without IL-1 β for 24 h. Representative immunofluorescence staining for (A) ZO-1 and (B) connexin 43. Scale bar, 50 μ m. Quantitative analysis of (C) ZO-1 and (D) connexin 43 fluorescence intensity. Reverse transcription-quantitative PCR detection of (E) ZO-1 and (F) connexin 43 mRNA expression. n=5. (G) Western blotting for (H) ZO-1 and (I) connexin 43 protein expression. (J) Immunofluorescence staining of EC cytoskeletal actin (dashed lines). (K) Immunofluorescence staining for VE-cadherin (arrow). Scale bar, 20 μ m. (L) Proliferation of ECs in scratch assay. Scale bar, 500 μ m. (M) Quantitative analysis of migration area in EC scratch assay. n=3. **P<0.01 and ***P<0.001. RhoA, Ras homolog family member A; EC, endothelial cell; LV-RhoA, Lentiviral vectors-RhoA; ZO-1, Zona occludens-1; VE-, vascular endothelial-cadherin.

branched actin filaments. However, RhoA knockdown ameliorated these IL-1 β -induced changes in the cytoskeleton (Fig. 3J). RhoA knockdown reversed IL-1 β -induced alterations in VE-cadherin distribution along EC junctions (Fig. 3K). Moreover, cell scratch assay indicated that RhoA knockdown attenuated IL-1 β -induced inhibition of cell migration (Fig. 3L and M). Collectively, these results suggested that RhoA suppression may ameliorate IL-1 β -induced increase in vascular permeability in ECs.

Ferroptosis enhances vascular permeability in ECs. The present study confirmed the inhibitory effect of ferrostatin-1 on ferroptosis in IL-1 β -treated ECs. Immunofluorescence staining showed that ferrostatin-1-induced inhibition of ferroptosis significantly reversed IL-1 β -induced decrease in the average fluorescence intensity of GPX4 (Fig. S6A and C). By contrast, ferrostatin-1-induced inhibition of ferroptosis decreased the average fluorescence intensity of ACSL4 in ECs (Fig. S6B and D). Additionally, RT-qPCR indicated that ferrostatin-1-induced inhibition of ferroptosis significantly reversed IL-1 β -induced decrease in mRNA expression of SLC7A11 and GPX4 in ECs and decreased mRNA expression of ACSL4 (Fig. S6E-G), which was confirmed by western blot analysis (Fig. S6H-K). ferroptosis inhibition effectively reversed IL-1 β -induced increases in ROS levels and increased mitochondrial membrane potential (Fig. S6L-N). The present study investigated the effects of ferrostatin-1-induced inhibition of ferroptosis on vascular permeability in IL-1 β -treated ECs. Immunofluorescence staining showed that, compared with IL-1 β -treated ECs, ferrostatin-1-induced inhibition of ferroptosis restored ZO-1 and connexin 43 fluorescence intensity in IL-1 β -treated ECs (Fig. 4A-D). RT-qPCR indicated that ferroptosis inhibition enhanced IL-1 β -induced downregulation of ZO-1 and connexin 43 mRNA expression in ECs (Fig. 4E and F), which was confirmed by western blotting (Fig. 4G-I). Moreover, ferroptosis inhibition ameliorated IL-1 β -induced decrease in stress fibers and decreased branched actin filaments in ECs (Fig. 4J). Furthermore, ferroptosis inhibition reversed IL-1 β -induced alteration in VE-cadherin distribution along the EC junction (Fig. 4K). The scratch assay showed that ferroptosis inhibition reversed the IL-1 β -induced decrease in cell migration (Fig. 4L and M). Collectively, these results suggested that ferroptosis inhibition may mitigate IL-1 β -induced increase in vascular permeability in ECs.

RhoA regulates ferroptosis in ECs. To investigate the potential mechanism by which RhoA influences vascular permeability, the present study examined the effects of RhoA inhibition on ferroptosis in IL-1 β -treated ECs. The SLC7A11/GPX4 antioxidant system and ACSL4 are key in the regulation of ferroptosis (33,34). Immunofluorescence staining showed that RhoA knockdown significantly reversed IL-1 β -induced decrease in the mean fluorescence intensity of GPX4 (Fig. 5A and C). By contrast, RhoA knockdown decreased the mean fluorescence intensity of ACSL4 in ECs (Fig. 5B and D). Additionally, RT-qPCR indicated that RhoA knockdown significantly reversed IL-1 β -induced decrease in mRNA expression of SLC7A11 and GPX4 in ECs and decreased the mRNA expression of ACSL4 (Fig. 5E-G), which was confirmed by western blot analysis (Fig. 5H-K).

To ascertain the role of RhoA in ferroptosis, the present study assessed lipid ROS levels and mitochondrial membrane potential in ECs. IL-1 β treatment significantly increased ROS levels in ECs and markedly decreased mitochondrial membrane potential, as indicated by immunofluorescence staining. However, RhoA inhibition effectively reversed IL-1 β -induced increases in ROS levels and increased mitochondrial membrane potential (Fig. 5L-N). Overall, these results indicated that RhoA regulated ferroptosis by affecting mitochondrial function and oxidative stress.

RhoA affects vascular permeability via ferroptosis in ECs. To confirm the role of ferroptosis in RhoA-mediated regulation of permeability in IL-1 β -treated ECs, the present study simultaneously inhibited RhoA and activated ferroptosis in ECs. Immunofluorescence staining showed that RhoA inhibition notably enhanced fluorescence intensity of ZO-1 and connexin 43 in IL-1 β -treated ECs; however, ferroptosis activation counteracted these effects (Fig. 6A-D). RT-qPCR indicated that ferroptosis activation nullified RhoA inhibition-induced increase in ZO-1 and connexin 43 mRNA expression in IL-1 β -treated ECs (Fig. 6E and F). Additionally, immunofluorescence staining indicated that RhoA knockdown rescued IL-1 β -induced decrease in stress fibers and decreased branched actin filaments in ECs; however, these changes were reversed by ferroptosis activation (Fig. 6G). Moreover, ferroptosis activation nullified RhoA knockdown-induced amelioration of alterations in VE-cadherin distribution along junctions in IL-1 β -treated ECs (Fig. 6H). Wound healing assay showed that ferroptosis counteracted RhoA knockdown-induced decrease in migration in IL-1 β -treated ECs (Fig. 6I and J). Overall, these results indicated that RhoA influenced vascular permeability in ECs via ferroptosis.

RhoA enhances ferroptosis in DMM mice. To assess the role of RhoA and ferroptosis in OA, the present study established a murine model of OA via DMM and evaluated the toxicity of rhosin and ferrostatin-1 8 weeks post-DMM. Rhosin and ferrostatin-1 had minimal effect on the body weight, liver, kidney and spleen of mice at 8 weeks post-DMM (Fig. S7A-D). Hepatic lobules exhibited intact and well-organized tissue structure, the spleen structure appeared largely normal, and there were no evident pathological alterations in the glomerular and tubular structures of the kidneys. Additionally, parameters, including biochemical indices at 4 and 8 weeks post-DMM, were evaluated to assess the potential toxicity of ferrostatin-1 and rhosin. Notably, there were no significant differences in blood sugar levels (GSP and GLU), liver function (ALB, DBIL and TBA), renal function (CRE, UA, and UREA), and myocardial enzyme activity (CK, CK-MB, LDH and HBDH) between groups (Figs. S8A-H and S9A-D). Collectively, these results suggested that RhoA and ferroptosis inhibition did not induce toxic effects in mice.

Lipid peroxidation and mitochondrial dysfunction are key components of ferroptosis (35). Therefore, the present study investigated the effects of RhoA and ferroptosis on lipid metabolism and antioxidant capacity in mice at 4 and 8 weeks post-DMM. Triglyceride (TG), total cholesterol (TC), low-density lipoprotein cholesterol (LDL-C), high-density lipoprotein (HDL-C), malondialdehyde

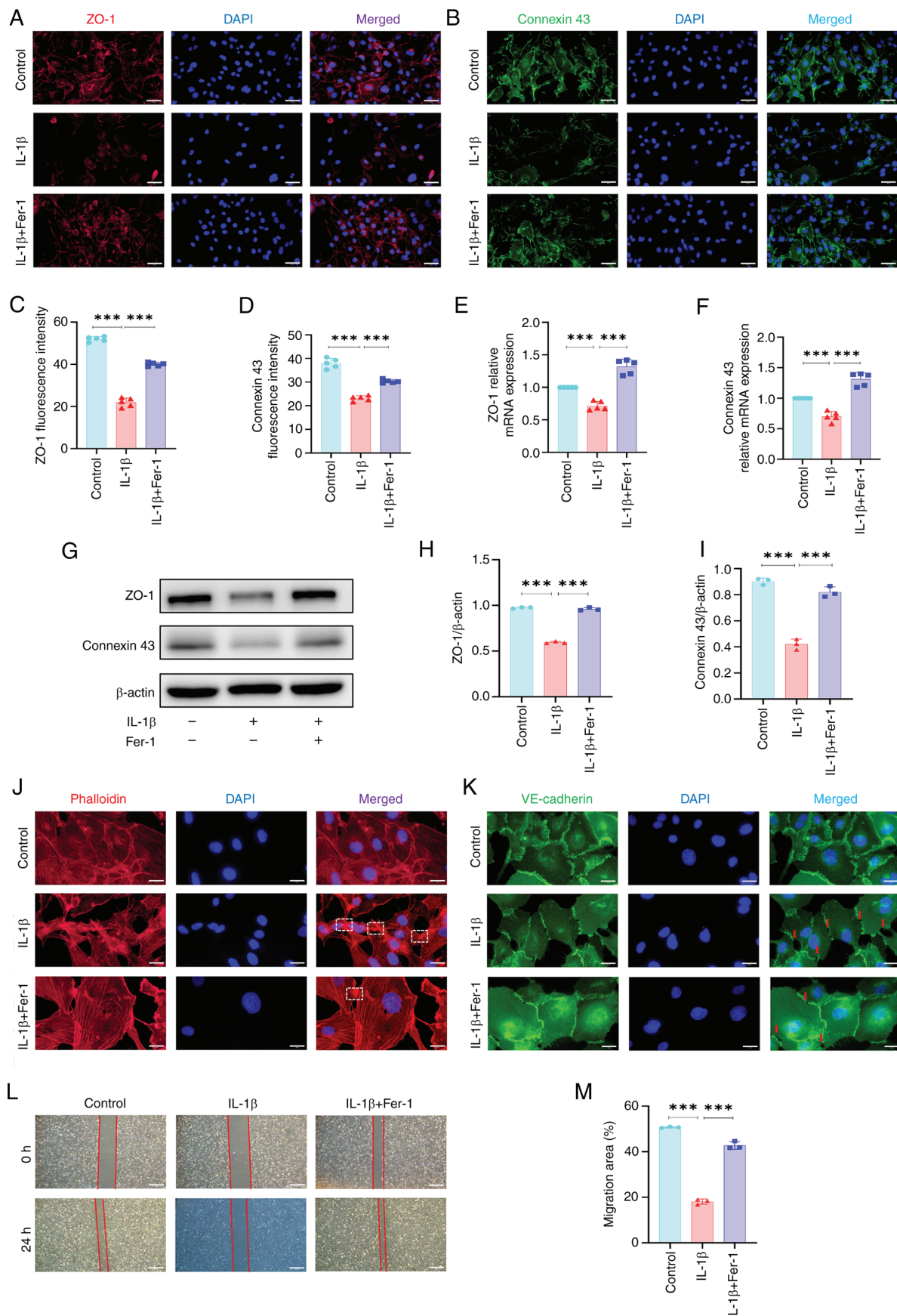


Figure 4. Ferropoptosis inhibition reverses IL-1 β -induced increase in EC permeability. ECs were incubated with IL-1 β alone or combination with Fer-1 for 24 h. Representative immunofluorescence staining for (A) ZO-1 and (B) connexin 43. Scale bar, 50 μ m. Quantitative analysis of (C) ZO-1 and (D) connexin 43 fluorescence intensity. Reverse transcription-quantitative PCR to detect (E) ZO-1 and (F) connexin 43 mRNA expression. n=5. (G) Western blotting for (H) ZO-1 and (I) connexin 43 protein expression. (J) Immunofluorescence staining for EC cytoskeletal F-actin (dashed line). (K) Immunofluorescence staining for VE-cadherin (arrow). Scale bar, 20 μ m. (L) Migration of ECs in scratch assay. Scale bar, 500 μ m. (M) Quantitative analysis of cell migration in scratch assay. n=3. ***P<0.001. EC, endothelial cell; Fer-1, Ferrostatin-1; ZO-1, Zona occludens-1; VE-, vascular endothelial-cadherin.

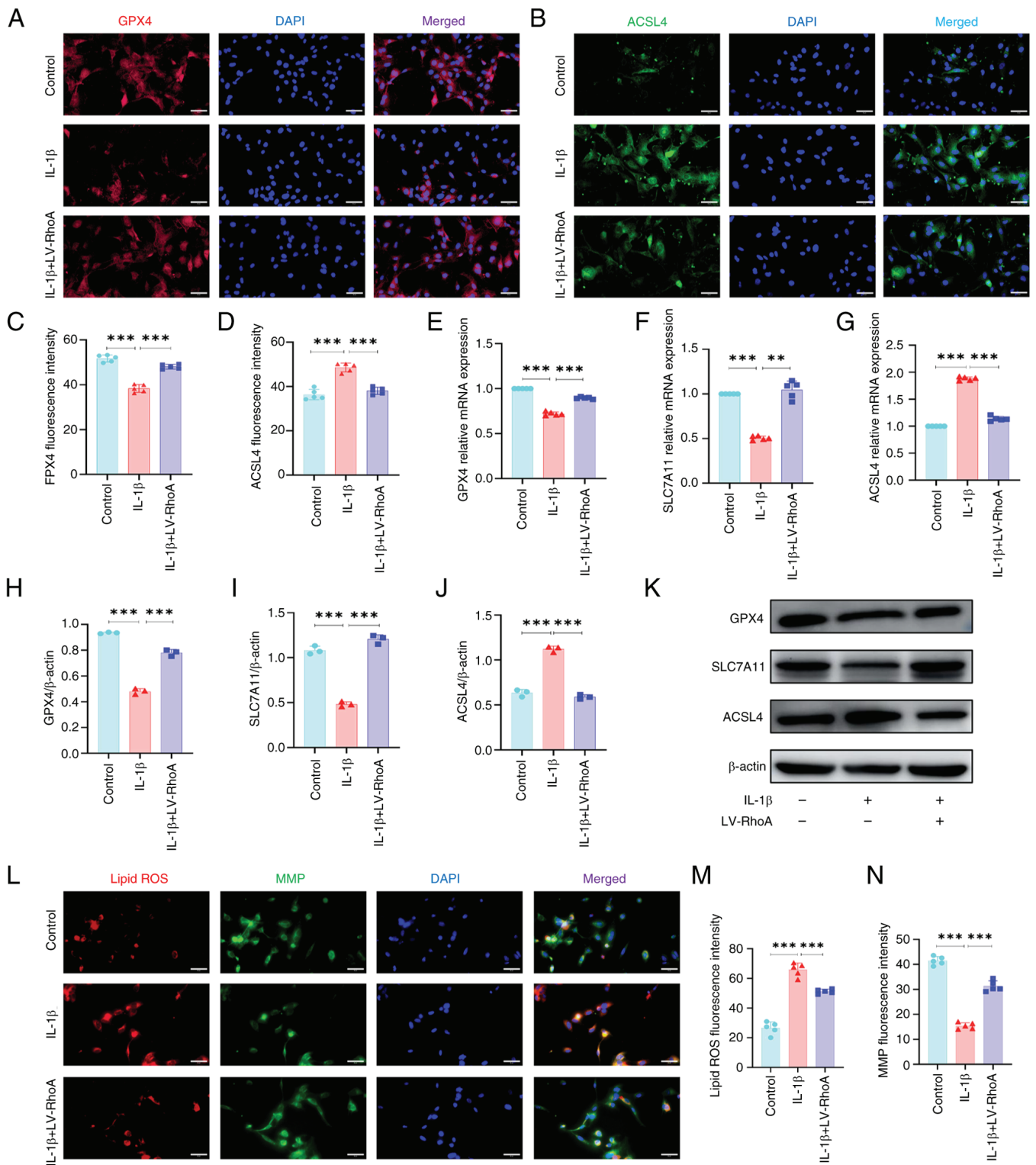


Figure 5. RhoA inhibition reverses IL-1 β -induced increase ferroptosis in ECs. ECs were transfected with LV-RhoA and treated with or without IL-1 β for 24 h. Representative immunofluorescence staining for (A) GPX4 and (B) ACSL4. Scale bar, 50 μ m. Quantitative analysis of (C) GPX4 and (D) ACSL4 fluorescence intensity. Reverse transcription-quantitative PCR to detect (E) GPX4, (F) SLC7A11 and (G) ACSL4 mRNA expression. n=5. Quantitative analysis of (H) GPX4, (I) SLC7A11 and (J) ACSL4 protein expression. n=3. (K) Western blotting for GPX4, SLC7A11 and ACSL4 protein expression. (L) Assessment of (M) ROS and (N) MMP in ECs. Scale bar, 50 μ m. n=5. **P<0.01 and ***P<0.001. RhoA, Ras homolog family member A; EC, Endothelial cell; LV-RhoA, Lentiviral vectors-RhoA; GPX4, Glutathione peroxidase 4; ACSL4, Acyl-CoA synthase long-chain family member 4; SLC7A11, Solute carrier family 7 member 11; ROS, reactive oxygen species; MMP, mitochondrial membrane potential.

(MDA) and nitric oxide (NO) levels, superoxide dismutase (SOD) and glutathione (GSH) activity and total antioxidant capacity (T-AOC) were assessed. Compared with the

sham group, there was a significant increase in TG, TC and LDL-C levels and a decrease in HDL-C levels in the DMM group. However, inhibition of ferroptosis and RhoA

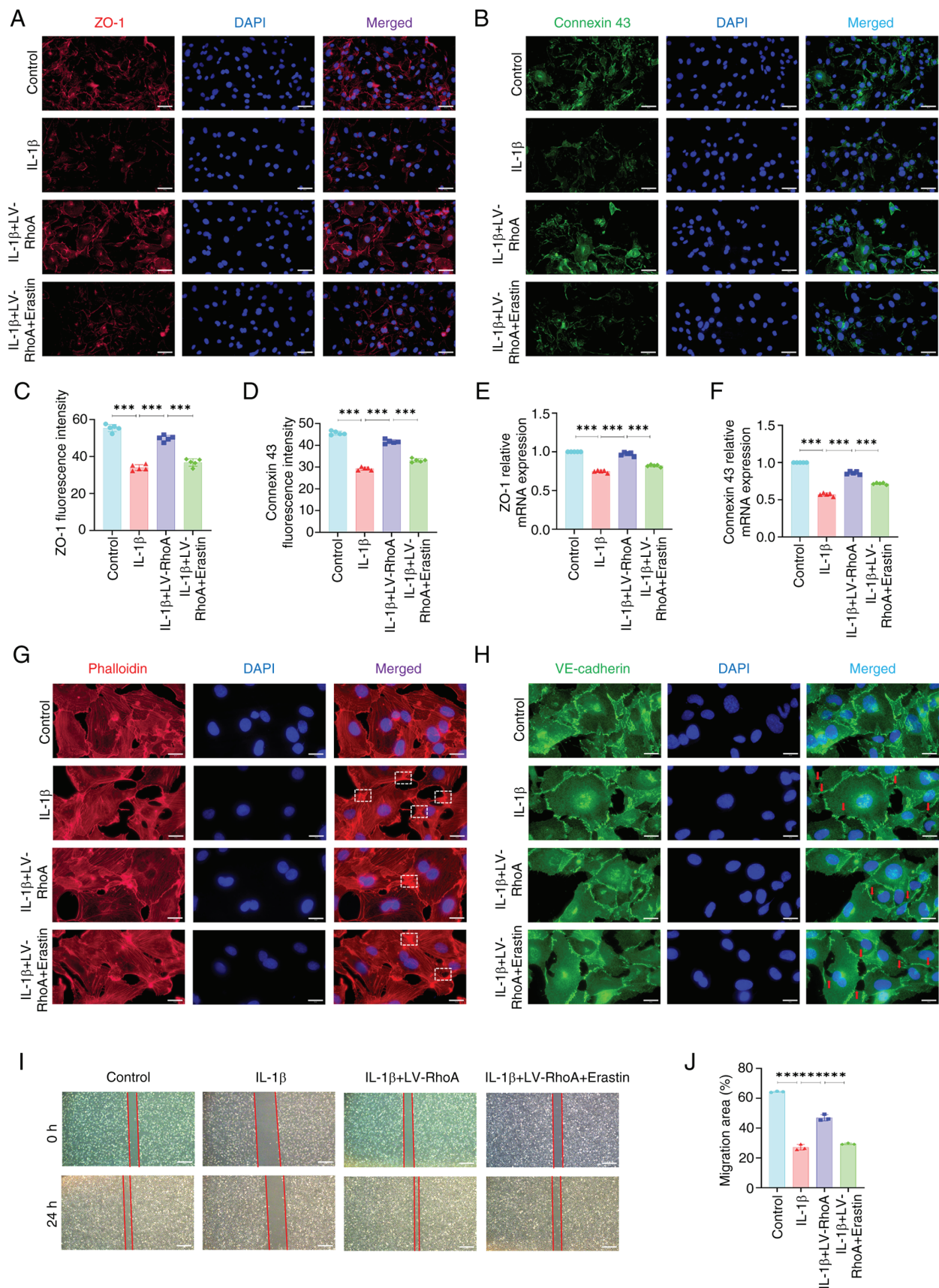


Figure 6. Ferropoptosis reverses the protective effect of RhoA knockdown on permeability in IL-1 β -treated ECs. ECs were transfected with LV-RhoA and treated with IL-1 β alone or combination with erastin for 24 h. Representative immunofluorescence staining for (A) ZO-1 and (B) connexin 43. Scale bar, 50 μ m. Quantitative analysis of (C) ZO-1 and (D) connexin 43 fluorescence intensity. Reverse transcription-quantitative PCR to detect (E) ZO-1 and (F) connexin 43 mRNA expression. n=5. (G) Immunofluorescence staining for cytoskeleton in ECs. Dashed lines indicate branching actin filaments. (H) Immunofluorescence staining for VE-cadherin. Arrows indicate discontinuous distribution of VE-cadherin in the cell membrane. Scale bar, 20 μ m. (I) Migration of ECs in scratch assay. Scale bar, 500 μ m. (J) Quantitative analysis of migration area in scratch assay. n=3. ***P<0.001. RhoA, Ras homolog family member A; EC, endothelial cell; LV, Lentiviral vectors-RhoA; ZO-1, Zona occludens-1; VE -, vascular endothelial-cadherin.

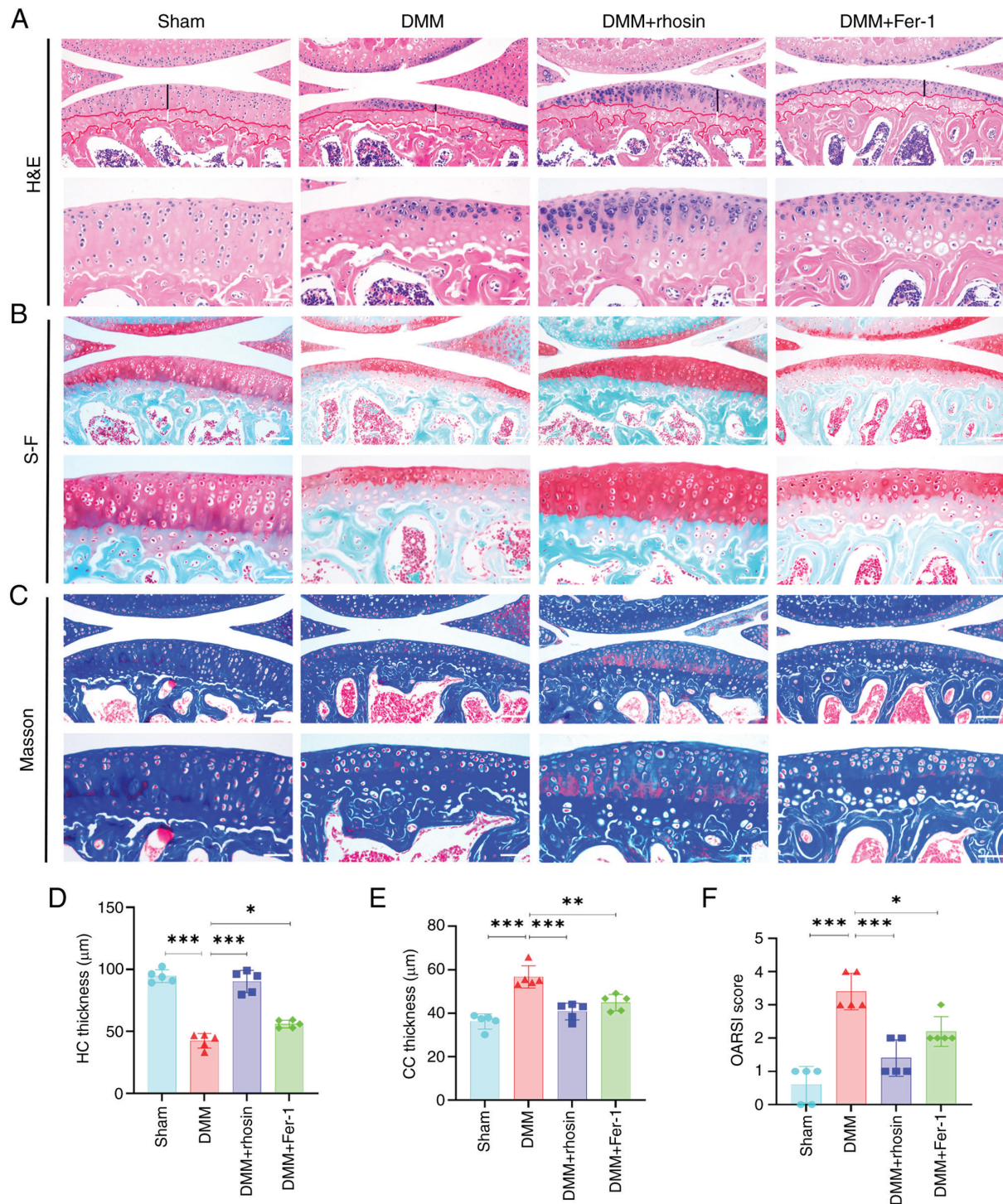


Figure 7. RhoA or ferroptosis inhibition alleviates cartilage degeneration in mice with DMM. (A) H&E, (B) S-F and (C) Masson's staining of knee joints in DMM mice after RhoA or ferroptosis inhibition. Black line, HC thickness; white, CC. Scale bar, 100 and 50 μm . Quantitative analysis of (D) HC and (E) CC thickness in H&E-stained samples and (F) OARSI scores of knee joint cartilage using S-F staining. $n=5$. * $P<0.05$, ** $P<0.01$ and *** $P<0.001$. RhoA, Ras homolog family member A; DMM, destabilization of the medial meniscus; H&E, hematoxylin and eosin; S-F, Safranin-O-fast green; HC, Hyaline cartilage; CC, Calcified cartilage; OARSI, Osteoarthritis Research Society International; Fer-1, Ferrostatin-1.

effectively mitigated these alterations, suggesting that RhoA and ferroptosis inhibition may modulate blood lipid metabolism in DMM mice (Fig. S9E-H). Additionally, there was an increase in MDA levels and a decrease in SOD, GSH and T-AOC in the DMM group compared with the sham group. However, ferrostatin-1 and rhosin effectively reversed DMM-associated changes in MDA levels, SOD and GSH

activity and T-AOC (Fig. S9I-L). Overall, these results indicated that the inhibition of RhoA and ferroptosis enhanced antioxidant capacity in DMM mice.

Inhibition of RhoA ameliorates progress of OA in DMM mice. To determine the effect of RhoA on OA *in vivo*, OA progression in mice 8 weeks post-DMM was assessed using

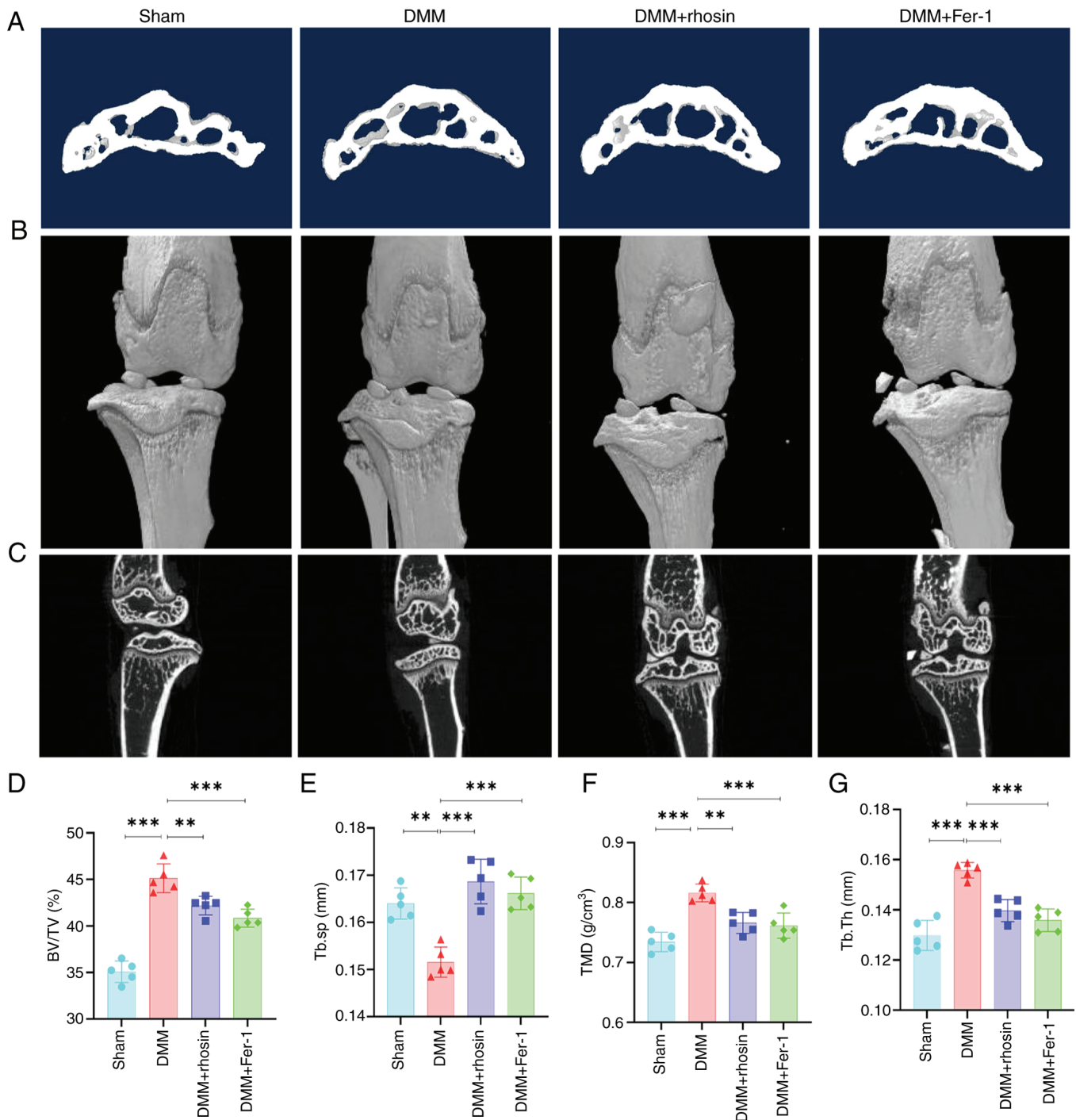


Figure 8. RhoA or ferroptosis inhibition rescues subchondral bone remodeling in DMM mice. (A) Two-dimensional micro-CT scan of the tibial subchondral bone. Magnification: $\times 10$. (B) Representative three-dimensional micro-CT reconstructed images of mouse knee joints. Magnification: $\times 10$. (C) Two-dimensional micro-CT reconstruction of the tibial subchondral bone. Magnification: $\times 10$. (D) BV/TV. (E) Tb.Sp. (F) TMD. (G) Tb.Th. $n=5$. ** $P<0.01$ and *** $P<0.001$. RhoA, Ras homolog family member A; DMM, destabilization of the medial meniscus; CT, micro-computed tomography; BV/TV, bone volume/total volume; Tb.Sp, trabecular separation; TMD, tissue mineral density; Tb.Th, trabecular thickness; Fer-1, Ferrostatin-1.

H&E, safranin-O-fast green and Masson staining. The MM of mice in the sham group was characterized by intact and smooth articular cartilage surface, moderate cartilage thickness, distinct tidemark, a substantial number of chondrocytes and a normal chondrocyte structure and size (Fig. 7A-C). However, articular cartilage damage, decreased cartilage thickness, reduced chondrocyte count, abnormal chondrocyte size and structure, disappearance of hyaline cartilage (HC), and a significant increase in calcified cartilage (CC) were

observed 8 weeks after DMM. Notably, these changes were largely reversed in the rhosin-treated group (Fig. 7A, D and E). Additionally, OARSI histological score was used to evaluate sections stained with safranin-O-fast green. Compared with the sham group, the OARSI score was significantly higher in the DMM group. However, rhosin treatment inhibited the increase in the OARSI score observed in DMM mice (Fig. 7B and F). Overall, these results suggested that RhoA inhibition ameliorated OA progression in DMM mice.

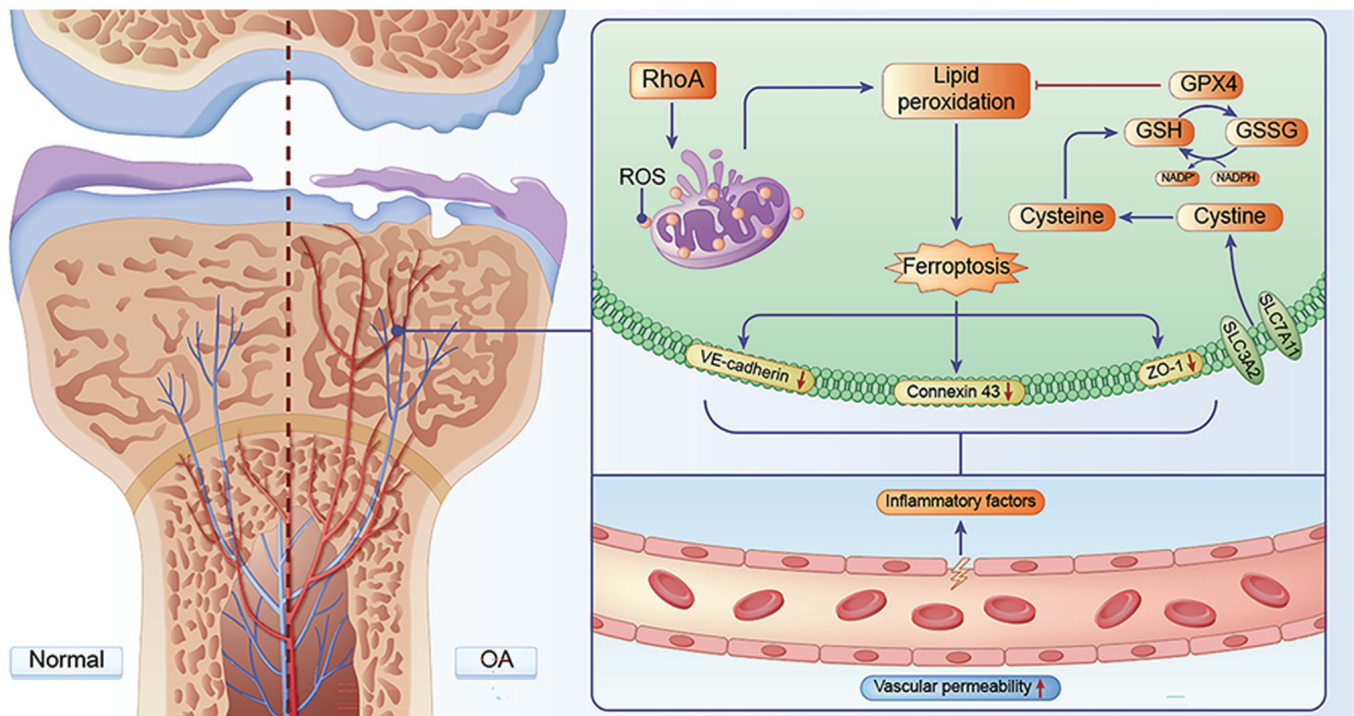


Figure 9. Potential mechanism of RhoA in OA. RhoA increases vascular permeability in osteoarthritis through ferroptosis. RhoA, Ras homolog family member A; OA, osteoarthritis; ROS, reactive oxygen species; GPX4, Glutathione peroxidase 4; GSH, Glutathione; GSSG, Oxidized glutathione; VE, vascular endothelial-cadherin; ZO-1, Zona occludens-1; SLC7A11, Solute carrier family 7 member 11.

Micro-CT scan was performed on subchondral bone of DMM mice to elucidate the role of RhoA in OA. Notable osteophyte formation was observed in the DMM group, which was notably ameliorated by RhoA inhibition (Fig. 8A-C). Additionally, subchondral sclerosis was indicated by increased BV/TV, Tb.Th and TMD and reduced Tb.Sp in DMM mice. However, RhoA inhibition partially mitigated these alterations (Fig. 8D-G). Collectively, these results indicated that RhoA inhibition improved subchondral bone remodeling in mice after DMM surgery.

Inhibition of ferroptosis improves OA progression in DMM mice. Ferroptosis inhibition mitigated cartilage damage and enhanced OARSI score in DMM mice (Fig. 7A-F). Micro-CT scan indicated osteophyte formation 8 weeks post-DMM surgery; however, ferroptosis inhibition significantly reversed osteophyte development. Additionally, ferroptosis inhibition significantly reversed OA-associated subchondral sclerosis in DMM mice, evidenced by a decrease in BV/TV, Tb.Th and TMD and an increase in Tb.Sp (Fig. 8D-G). Overall, these results suggested that ferroptosis inhibition ameliorated the progression of OA.

Discussion

During onset and progression of OA, subchondral bone exhibits abnormal neovascularization and enhanced vascular permeability (36). However, the molecular mechanisms underlying increased vascular permeability in OA remain unclear. Considering the pathogenesis of OA, identifying and developing effective strategies to mitigate vascular permeability may be effective for OA prevention and treatment. In the present study,

proteomic analysis indicated that RhoA was significantly upregulated in subchondral bone of patients with OA. RhoA is a Rho GTPase involved in biological activities, including cell proliferation, apoptosis, migration and invasion (37). Research indicates that RhoA can suppress the expression of several adhesion molecules such as ZO-1, Connexin 43 in ECs, thereby increasing vascular permeability (38). Additionally, RhoA mediates OA progression by affects cartilage degeneration. Notably, chondrocyte cytoskeleton remodeling is directly related to the progression of OA and is characterized by the RhoA/Rock pathway activation-induced chondrocyte cytoskeleton reorganization, changes in cell shape, and stress fiber formation (39). Additionally, RhoA mediates Wnt/ β -catenin regulation of chondrocyte catabolism, hypertrophy, and cartilage degradation (40). However, the role of RhoA in the vascular permeability of the subchondral bone in OA is poorly understood. However, the role of RhoA in the vascular permeability of the subchondral bone in OA is poorly understood. In the present study, high RhoA expression was associated with increased vascular permeability of the subchondral bone in patients with OA. Therefore, it is crucial to investigate the association between RhoA and vascular permeability of the subchondral bone in OA.

RhoA can affect blood-brain barrier permeability by regulating tight junction proteins (41). Moreover, RhoA adjusts EC permeability by enhancing actin filaments (42). The contraction force generated by branched actin filaments widens the gap between cells, thereby increasing permeability. Here, proteomic and bioinformatics analyses indicated an association between RhoA, ferroptosis and vascular permeability in OA. Additionally, *in vitro* experiments showed that RhoA inhibition reversed IL-1 β -induced increase in vascular

permeability in ECs and DMM mice. Moreover, RhoA inhibition suppressed lipid metabolism and activated the antioxidant system in DMM mice. Overall, these findings suggested that RhoA may regulate vascular permeability by mediating ferroptosis. RhoA inhibition suppressed ferroptosis by activating the antioxidant system and suppressing lipid peroxidation *in vitro*, which was confirmed by the results of biochemical analysis of mouse serum. Additionally, RhoA inhibition ameliorated IL-1 β -induced decrease in mitochondrial membrane potential in ECs. Therefore, it was hypothesized that RhoA may decrease in mitochondrial membrane potential, thereby elevating ROS production in the cytoplasm, promoting lipid peroxidation, inhibiting the antioxidant system and inducing ferroptosis.

Many studies have shown that ferroptosis is involved in the damage and degeneration of chondrocytes, thereby inducing the progression of osteoarthritis (43,44). Various drugs, including astaxanthin and biochanin A, alleviate cartilage degeneration in osteoarthritis by inhibiting ferroptosis (45,46). Additionally, ferroptosis is involved in the death of endothelial cells and changes in vascular permeability. However, the exact role of ferroptosis in the vascular permeability of subchondral bone in osteoarthritis remains unclear. To elucidate the effect of ferroptosis on vascular permeability of subchondral bone in OA, *in vitro* and *in vivo* experiments were performed using a ferroptosis inhibitor/activator. Ferroptosis inhibition effectively maintained the permeability of ECs, whereas ferroptosis activation reversed the protective effects of RhoA inhibition on EC permeability. Similarly, *in vivo* experiments showed that ferroptosis inhibition ameliorated subchondral bone sclerosis and remodeling in DMM mice. Mechanistically, RhoA inhibition-induced decrease in ferroptosis and improvement in vascular permeability may be primarily attributed to suppression of oxidative stress and enhancement of mitochondrial function. IL-1 β -induced increase in ROS generation and mitochondrial dysfunction in ECs may increase permeability. By contrast, inhibiting ROS generation may regulate cell permeability and inflammatory response (47). Lipid metabolism may also be involved in oxidative stress- and mitochondrial dysfunction-induced increase in vascular permeability. Systemic inflammation is characterized by an increase in ROS production, which can upregulate oxidized HDL and nullify the protective effects of non-oxidized HDL on blood vessels. Additionally, ROS can promote endothelial fibrosis, resulting in downregulation of adhesion proteins, thereby compromising endothelial integrity and increasing permeability (48).

In conclusion, the present study demonstrated that RhoA can effectively induce OA progression by modulating ferroptosis and vascular permeability. Specifically, RhoA disrupted mitochondrial function in ECs, leading to oxidative stress. Excessive ROS production can induce ferroptosis in ECs and inhibit expression of cell adhesion proteins, such as ZO-1, connexin 43 and VE-cadherin, thereby damaging inter-EC connections and increasing vascular permeability. Excessive release of inflammatory factors from newly formed blood vessels contributes to the progression of OA (Fig. 9). Moreover, RhoA may be a potential key target for treating OA in future, thus presenting a novel therapeutic approach for OA treatment. Although inhibiting RhoA and ferroptosis effectively alleviated cartilage degeneration and subchondral bone remodeling,

thereby improving the progression of OA *in vivo*, further study is required to elucidate the mechanism.

Acknowledgements

Not applicable.

Funding

The present study was supported by National Natural Science Foundation of China (grant nos. U22A20285, 82160433 and 82360319), Key R&D Project of Autonomous Region (grant nos. 2023BEG02018, 2021BEG02037 and 2022BEG03126), Scientific Research Project of Ningxia University (grant no. NYG-2022033) and Ningxia Medical University General Hospital 'Medical Engineering Special' (grant no. NYZYYG-001).

Availability of data and materials

The data generated in the present study may be found in the ProteomeXchange Consortium via the iProX partner repository under accession number PXD051627 or at the following URL: proteomexchange.org.

Authors' contributions

QJ, DX and XH designed the study. XH, KT, XL, XC, YS and LM performed experiments. ZLu, ZC, LZ and PL analyzed data. GF, XZ, ZLa and CZ analyzed and interpreted data and wrote the manuscript. XH and KT confirm the authenticity of all the raw data. All authors have read and approved the final manuscript.

Ethics approval and consent to participate

The present study was approved by the Ethics Committee of the General Hospital of Ningxia Medical University, China (approval no. KYLL-2021-269). The study adhered to the Helsinki Declaration. Written informed consent provided was by the patients. All animal experiment procedures were executed in compliance with the Guidelines for the Care and Use of Laboratory Animals by the National Institutes of Health and were approved by the Animal Ethics Committee of Ningxia Medical University, China (approval no. IACUC-NY LAC-2023-100).

Patient consent for publication

The patients provided written informed consent regarding the publication of the case details and associated images.

Competing interests

The authors declare that they have no competing interests.

References

1. Glyn-Jones S, Palmer AJ, Agricola R, Price AJ, Vincent TL, Weinans H and Carr AJ: Osteoarthritis. *Lancet* 386: 376-387, 2015.

2. Hunter DJ and Bierma-Zeinstra S: Osteoarthritis. *Lancet* 393: 1745-1759, 2019.
3. Mapp PI and Walsh DA: Mechanisms and targets of angiogenesis and nerve growth in osteoarthritis. *Nat Rev Rheumatol* 8: 390-398, 2012.
4. Walsh DA, McWilliams DF, Turley MJ, Dixon MR, Fransès RE, Mapp PI and Wilson D: Angiogenesis and nerve growth factor at the osteochondral junction in rheumatoid arthritis and osteoarthritis. *Rheumatology (Oxford)* 49: 1852-1861, 2010.
5. Ni R, Guo XE, Yan C and Wen C: Hemodynamic stress shapes subchondral bone in osteoarthritis: An emerging hypothesis. *J Orthop Translat* 32: 85-90, 2021.
6. Peng Y, Wu S, Li Y and Crane JL: Type H blood vessels in bone modeling and remodeling. *Theranostics* 10: 426-436, 2020.
7. Adzraku SY, Wang G, Cao C, Bao Y, Wang Y, Smith AO, Du Y, Wang H, Li Y, Xu K, *et al*: Robo4 inhibits gamma radiation-induced permeability of a murine microvascular endothelial cell by regulating the junctions. *Cell Mol Biol Lett* 28: 2, 2023.
8. Qian T, Qi B, Fei Y, Li J, Luo L, Lv B, Song Y, Sheng S, Xiao W, Huang X and Wang X: PLD2 deletion alleviates disruption of tight junctions in sepsis-induced ALI by regulating PA/STAT3 phosphorylation pathway. *Int Immunopharmacol* 114: 109561, 2023.
9. Arnold TR, Stephenson RE and Miller AL: Rho GTPases and actomyosin: Partners in regulating epithelial cell-cell junction structure and function. *Exp Cell Res* 358: 20-30, 2017.
10. Ridley AJ: Rho family proteins: Coordinating cell responses. *Trends Cell Biol* 11: 471-477, 2001.
11. Zhao H, Kong H, Wang W, Chen T, Zhang Y, Zhu J, Feng D and Cui Y: High glucose aggravates retinal endothelial cell dysfunction by activating the RhoA/ROCK1/pMLC/Connexin43 signaling pathway. *Invest Ophthalmol Vis Sci* 63: 22, 2022.
12. Chen J, Shi W, Xu Y, Zhang H and Chen B: Hirudin prevents vascular endothelial cell apoptosis and permeability enhancement induced by the serum from rat with chronic renal failure through inhibiting RhoA/ROCK signaling pathway. *Drug Dev Res* 82: 553-561, 2021.
13. Dixon SJ, Lemberg KM, Lamprecht MR, Skouta R, Zaitsev EM, Gleason CE, Patel DN, Bauer AJ, Cantley AM, Yang WS, *et al*: Ferroptosis: An iron-dependent form of nonapoptotic cell death. *Cell* 149: 1060-1072, 2012.
14. Miao Y, Chen Y, Xue F, Liu K, Zhu B, Gao J, Yin J, Zhang C and Li G: Contribution of ferroptosis and GPX4's dual functions to osteoarthritis progression. *EBioMedicine* 76: 103847, 2022.
15. Zhang S, Xu J, Si H, Wu Y, Zhou S and Shen B: The role played by ferroptosis in osteoarthritis: Evidence based on iron dyshomeostasis and lipid peroxidation. *Antioxidants (Basel)* 11: 1668, 2022.
16. Fei Y, Huang X, Ning F, Qian T, Cui J, Wang X and Huang X: NETs induce ferroptosis of endothelial cells in LPS-ALI through SDC-1/HS and downstream pathways. *Biomed Pharmacother* 175: 116621, 2024.
17. Li W, Zhao X, Zhang R, Liu X, Qi Z, Zhang Y, Yang W, Pang Y, Zhao C, Fan B, *et al*: Ferroptosis inhibition protects vascular endothelial cells and maintains integrity of the blood-spinal cord barrier after spinal cord injury. *Neural Regen Res* 18: 2474-2481, 2023.
18. Gu Y, Hao S, Liu K, Gao M, Lu B, Sheng F, Zhang L, Xu Y, Wu D, Han Y, *et al*: Airborne fine particulate matter (PM_{2.5}) damages the inner blood-retinal barrier by inducing inflammation and ferroptosis in retinal vascular endothelial cells. *Sci Total Environ* 838: 156563, 2022.
19. Altman R, Asch E, Bloch D, Bole G, Borenstein D, Brandt K, Christy W, Cooke TD, Greenwald R, Hochberg M, *et al*: Development of criteria for the classification and reporting of osteoarthritis. Classification of osteoarthritis of the knee. Diagnostic and therapeutic criteria committee of the American Rheumatism Association. *Arthritis Rheum* 29: 1039-1049, 1986.
20. Yan J, Ding D, Feng G, Yang Y, Zhou Y, Ma L, Guo H, Lu Z and Jin Q: Metformin reduces chondrocyte pyroptosis in an osteoarthritis mouse model by inhibiting NLRP3 inflammasome activation. *Exp Ther Med* 23: 222, 2022.
21. Francis TC, Gaynor A, Chandra R, Fox ME and Lobo MK: The selective RhoA inhibitor rhosin promotes stress resiliency through enhancing D1-medium spiny neuron plasticity and reducing hyperexcitability. *Biol Psychiatry* 85: 1001-1010, 2019.
22. Guerrero-Hue M, García-Caballero C, Palomino-Antolín A, Rubio-Navarro A, Vázquez-Carballo C, Herencia C, Martín-Sánchez D, Farré-Alins V, Egea J, Cannata P, *et al*: Curcumin reduces renal damage associated with rhabdomyolysis by decreasing ferroptosis-mediated cell death. *FASEB J* 33: 8961-8975, 2019.
23. Zhao YY, Yang YQ, Sheng HH, Tang Q, Han L, Wang SM and Wu WY: GPX4 plays a crucial role in Fuzheng Kang'ai decoction-induced non-small cell lung cancer cell ferroptosis. *Front Pharmacol* 13: 851680, 2022.
24. Jiang A, Xu P, Yang Z, Zhao Z, Tan Q, Li W, Song C, Dai H and Leng H: Increased Sparc release from subchondral osteoblasts promotes articular chondrocyte degeneration under estrogen withdrawal. *Osteoarthritis Cartilage* 31: 26-38, 2023.
25. Glasson SS, Chambers MG, Van Den Berg WB and Little CB: The OARSI histopathology initiative-recommendations for histological assessments of osteoarthritis in the mouse. *Osteoarthritis Cartilage* 18 (Suppl 3): S17-S23, 2010.
26. Ahola S and Langer T: Ferroptosis in mitochondrial cardiomyopathy. *Trends Cell Biol* 34: 150-160, 2024.
27. Cao L, Yang T, Huang S, Yun X, Hou H, Wang T, Shi D and Li X: Expression patterns of ZO-1/2 and their effects on porcine oocyte in vitro maturation and early embryonic development. *Theriogenology* 161: 262-270, 2021.
28. Schwyer C, Shamipour S, Pranjic-Ferscha K, Schauer A, Balda M, Tada M, Matter K and Heisenberg CP: Mechanosensation of tight junctions depends on ZO-1 phase separation and flow. *Cell* 179: 937-952.e18, 2019.
29. Liu X, Wang T, Wang W, Liang X, Mu Y, Xu Y, Bai J and Geng D: Emerging potential therapeutic targets of ferroptosis in skeletal diseases. *Oxid Med Cell Longev* 2022: 3112388, 2022.
30. Zeng H, Hou Y, Zhou X, Lang L, Luo H, Sun Y, Wan X, Yuan T, Wang R, Liu Y, *et al*: Cancer-associated fibroblasts facilitate premetastatic niche formation through lncRNA SNHG5-mediated angiogenesis and vascular permeability in breast cancer. *Theranostics* 12: 7351-7370, 2022.
31. Zhu Y: Gap junction-dependent and -independent functions of connexin43 in biology. *Biology (Basel)* 11: 283, 2022.
32. Liu J, Rickel A, Smith S, Hong Z and Wang C: 'Non-cytotoxic' doses of metal-organic framework nanoparticles increase endothelial permeability by inducing actin reorganization. *J Colloid Interface Sci* 634: 323-335, 2023.
33. Doll S, Proneth B, Tyurina YY, Panzilius E, Kobayashi S, Ingold I, Irmeler M, Beckers J, Aichler M, Walch A, *et al*: ACSL4 dictates ferroptosis sensitivity by shaping cellular lipid composition. *Nat Chem Biol* 13: 91-98, 2017.
34. Yang WS, SriRamaratnam R, Welsch ME, Shimada K, Skouta R, Viswanathan VS, Cheah JH, Clemons PA, Shamji AF, Clish CB, *et al*: Regulation of ferroptotic cancer cell death by GPX4. *Cell* 156: 317-331, 2014.
35. Jiang X, Stockwell BR and Conrad M: Ferroptosis: Mechanisms, biology and role in disease. *Nat Rev Mol Cell Biol* 22: 266-282, 2021.
36. Liu Y, Xie HQ and Shen B: Type H vessels-a bridge connecting subchondral bone remodelling and articular cartilage degeneration in osteoarthritis development. *Rheumatology (Oxford)* 62: 1436-1444, 2023.
37. Kempers L, Driessen AJM, van Rijssel J, Nolte MA and van Buul JD: The RhoGEF trio: A protein with a wide range of functions in the vascular endothelium. *Int J Mol Sci* 22: 10168, 2021.
38. Li L, Xin J, Wang H, Wang Y, Peng W, Sun N, Huang H, Zhou Y, Liu X, Lin Y, *et al*: Fluoride disrupts intestinal epithelial tight junction integrity through intracellular calcium-mediated RhoA/ROCK signaling and myosin light chain kinase. *Ecotoxicol Environ Saf* 257: 114940, 2023.
39. Yang J, Wang L, Zhang Z, Sun Q and Zhang Y: Downregulation of HAS-2 regulates the chondrocyte cytoskeleton and induces cartilage degeneration by activating the RhoA/ROCK signaling pathway. *Int J Mol Med* 52: 57, 2023.
40. Liang J, Feng J, Wu WK, Xiao J, Wu Z, Han D, Zhu Y and Qiu G: Leptin-mediated cytoskeletal remodeling in chondrocytes occurs via the RhoA/ROCK pathway. *J Orthop Res* 29: 369-374, 2011.
41. Feng S, Zou L, Wang H, He R, Liu K and Zhu H: RhoA/ROCK-2 pathway inhibition and tight junction protein upregulation by catalpol suppresses lipopolysaccharide-induced disruption of blood-brain barrier permeability. *Molecules* 23: 2371, 2018.
42. Dasgupta SK, Le A, Vijayan KV and Thiagarajan P: Dasatinib inhibits actin fiber reorganization and promotes endothelial cell permeability through RhoA-ROCK pathway. *Cancer Med* 6: 809-818, 2017.
43. Gao L, Hua W, Tian L, Zhou X, Wang D, Yang Y and Ni G: Molecular mechanism of ferroptosis in orthopedic diseases. *Cells* 11: 2979, 2022.
44. Yao X, Sun K, Yu S, Luo J, Guo J, Lin J, Wang G, Guo Z, Ye Y and Guo F: Chondrocyte ferroptosis contribute to the progression of osteoarthritis. *J Orthop Translat* 27: 33-43, 2020.

45. Wang X, Liu Z, Peng P, Gong Z, Huang J and Peng H: Astaxanthin attenuates osteoarthritis progression via inhibiting ferroptosis and regulating mitochondrial function in chondrocytes. *Chem Biol Interact* 366: 110148, 2022.
46. He Q, Yang J, Pan Z, Zhang G, Chen B, Li S, Xiao J, Tan F, Wang Z, Chen P and Wang H: Biochanin A protects against iron overload associated knee osteoarthritis via regulating iron levels and NRF2/System xc-/GPX4 axis. *Biomed Pharmacother* 157: 113915, 2023.
47. Qin X, Zhu L, Zhong Y, Wang Y, Wu G, Qiu J, Wang G, Qu K, Zhang K and Wu W: Spontaneously right-side-out-orientated coupling-driven ROS-sensitive nanoparticles on cell membrane inner leaflet for efficient renovation in vascular endothelial injury. *Adv Sci (Weinh)* 10: e2205093, 2023.
48. Rojas M, Prado Y, Tapia P, Carreño LJ, Cabello-Verrugio C and Simon F: Oxidized high-density lipoprotein induces endothelial fibrosis promoting hyperpermeability, hypotension, and increased mortality. *Antioxidants (Basel)* 11: 2469, 2022.



Copyright © 2024 He et al. This work is licensed under a Creative Commons Attribution-NonCommercial-NoDerivatives 4.0 International (CC BY-NC-ND 4.0) License.